Ultrasonics 150 (2025) 107599

Contents lists available at ScienceDirect

Ultrasonics

journal homepage: www.elsevier.com/locate/ultras

3D DEM modelling of acoustic emission in concrete: Insights into elastic waves initiated by microcracks

Michał Nitka [a], Magdalena Rucka [b,*]

[a] Department of Engineering Structures, Faculty of Civil and Environmental Engineering, Gdańsk University of Technology, Narutowicza 11/12 80-233 Gdańsk, Poland
[b] Department of Mechanics of Materials and Structures, Faculty of Civil and Environmental Engineering, Gdańsk University of Technology, Narutowicza 11/12 80-233 Gdańsk, Poland

ARTICLE INFO

Keywords:
Fracture monitoring
non-destructive testing (NDT)
discrete element method (DEM)
Acoustic emission
Concrete beams
Elastic waves
Micro-cracks

ABSTRACT

In this paper, 3-point bending concrete beams were investigated through a combination of experimental and numerical analyses. Initially, laboratory tests were conducted to observe the formation and propagation of cracks using acoustic emission (AE) and digital image correlation (DIC) techniques. The experimental results obtained were then compared with a numerical study. The widely used discrete element method (DEM), implemented with the open-source code YADE, was employed. The primary objective was numerically reproducing the acoustic emission experiment. The model was fully 3D. During the entire test, the accelerations of 4 sensors were monitored, mirroring the experimental setup. The energy released during the damage process was quantified, and both cumulative energy and local jumps were directly compared. Furthermore, energy measurements were correlated with stress curves to explore their interdependencies. The numerical model, along with the experimental measurements, successfully detected signals from the sensors, indicating the occurrence of microcracking in the specimen before reaching peak load and failure.

1. Introduction

The cracking process is a fundamental phenomenon observed in quasi-brittle and brittle materials ([1–3]), which refers to materials that fracture under stress without significant deformation. It stands as a primary cause of mechanical damage under load, leading to a significant reduction in material strength. Understanding the fracture process is paramount for ensuring structural safety and optimizing material behaviour. During the damage process, microcracks initially emerge in a hardening region before the peak on the stress–strain curve is reached. These micro-cracks gradually evolve during softening of the material, eventually transforming into distinct macroscopic cracks that lead to rupture [4]. Identifying microcracks in concrete elements before they lead to failure is a critical and complex engineering task. Early detecting these microfractures can significantly enhance the safety of structures.

In recent years, substantial advancements have been made in non-destructive evaluation techniques for concrete structures [5,6]. Additionally, numerous experimental studies have focused on the continuous observation of concrete elements as they degrade under progressively increasing mechanical loads [7–9]. Among the various techniques available, the acoustic emission (AE) method stands out as particularly effective for real-time, in-situ monitoring of microcrack development in concrete, e.g. [10–19]. This method detects the release of strain energy from cracks or excessive deformation, which generates elastic waves that travel through the material. Sensors placed on the surface of the specimen capture these AE events, providing valuable data on the initiation and growth of microcracks and fractures in stressed concrete samples [20,21,22]. However, most of the existing work focuses on laboratory tests only. There remains a gap in the numerical analysis of the interaction between elastic waves and developing fracture zones, particularly when compared to laboratory tests. Finite element methods (FEM) have been used to study these problems; however, they face

* Corresponding author.
E-mail addresses: michal.nitka@pg.edu.pl (M. Nitka), magdalena.rucka@pg.edu.pl (M. Rucka).

https://doi.org/10.1016/j.ultras.2025.107599
Received 16 September 2024; Received in revised form 22 November 2024; Accepted 10 February 2025
Available online 11 February 2025

challenges in accurately mimicking fragmentation and multi-cracking. Most numerical research has been limited to 2D applications only, which can introduce noticeable errors due to the inability to fully account for all spatial effects [23]. The constitutive laws used in FEM models are also generally complicated and do not fully capture the physics of fragmentation [24,25]. Zhu et al. [26] performed numerical simulations of the AE activity during the failure process of a concrete beam, considering the concrete as a heterogeneous material. Lisjak et al. [27] described a method for AE modelling based on a combined finite-discrete element method with cohesive elements, allowing for the modelling of fracture process zones (FPZs). However, real fracture problems involve multi-cracking, which is a significant challenge for continuous models. While finite element techniques are excellent tools for large-scale calculations, they are quite limited in computations on a *meso*-structure level.

The increasingly popular, discrete element method (DEM) can effectively address most of the issues mentioned above. DEM directly simulates the material *meso*-structure, making it suitable for comprehensive studies of the mechanisms behind the initiation, growth, and formation of localized zones, cracks, and fractures at the mesoscale, which significantly affect the macroscopic behaviour of frictional-cohesive materials [28,29]. It can easily represent discontinuities caused by fracturing or fragmentation. The accessibility of information at the particle scale makes DEM a highly useful tool for studying the growth of fracture zones and tracking elastic waves as the released energy. However, the major disadvantage of DEM is its high computational cost. Wave simulation in heterogeneous materials has been studied by many researchers, demonstrating the great potential and capabilities of this method. Studies have been conducted on wave propagation in 2D cohesionless granular media [30] and in porous asphalt [31]. However, there is still a lack of complex analysis of elastic wave propagation during concrete degradation. Most calculations focus on rocks and are limited to 2D problems. Hazzard and Young [32] simulated a compressive failure test on a granite sample model with simultaneous recording of AE signals. Ji and Di [33] applied simplified discrete element modelling (DEM) to study acoustic emission features in rock fractures. Unlike other studies, their work addressed a 3D problem, although it involved only about 6000 randomly placed particles. Chong et al. [34] numerically simulated the acoustic emission characteristics of a jointed rock mass using a 2D model. Zhang et al. [35] conducted compression tests on coal specimens and monitored the AE. They used two-dimensional numerical approach to calculate the number of cracks during biaxial compressive loading and compared it with the cumulative AE counts registered during the experiments. Several papers also describe cement or concrete materials. Iturrioz et al. [36] used a lattice model to describe experimental studies of fracture monitoring in concrete specimens based on AE. Cheng et al. [37] performed acoustic emission simulations of cemented tailings backfill, using 2D particle flow code to compare the number of microcracks from simulations with the magnitude of AE events from experiments. Zhu et al. [38] utilized a local crack opening displacement softening model within the framework of the discrete element method to study the fracture behaviour of concrete bending beams, comparing 2D numerical simulation results with experimental data from acoustic emission (AE) and digital image correlation (DIC) techniques. Similar work has been performed in our previous research [39]. Finally, a comprehensive numerical and experimental study on the failure analysis of porous concrete was presented by Xie et al. [40], using a 3D DEM model. Laboratory tests were conducted on specimens made from 10-25 mm aggregate bound with cement mortar. Acoustic emission (AE) events were recorded during these experiments. The numerical model included aggregate particles with linear parallel bonds between them, allowing the number of cracks formed during the compression of the porous concrete specimen to be counted and compared with the experimental cumulative AE energy curve.

In our study, the laboratory setup was designed to allow for the precise observation of crack initiation and propagation using the digital image correlation (DIC) technique, as well as the accurate measurement of elastic waves released from localizes sources during crack initiation and propagation by the acoustic emission (AE) technique using four piezoelectric sensors attached to concrete beams subjected to a mechanical degradation. Numerical simulations were then performed using the classical particle-based discrete element method (DEM). A full 3D model was built in DEM to closely mimic the experiment. The beam material was represented as a collection of individual particles, each capable of independent movement and interaction within the domain. DEM was selected over other discrete models due to its ability to accurately represent the concrete fracture process [41–43]. Due to the time-consuming nature of the calculations, a single-phase specimen was used, in contrast to the multi-phase approach presented in [39]. The focus was on the 3D extension to capture phenomena that could not be observed in 2D calculations. Finally, the experimental results were compared with numerical simulations to validate the accuracy of the model.

The main contribution of the current paper is a coupled experimental–numerical study to explain the mechanism of propagation of elastic waves at the aggregate-level and their interaction with micro- and macrocracking in concrete. The novelty of the work concerns (i) the development of a fully three-dimensional discrete element method model to simulate acoustic emissions in concrete members subjected to monotonic quasi-static loading, offering a detailed representation of the elastic wave propagation initiated by microcracks, and (ii) the establishment of a direct comparison between experimental measurements and numerical results, providing a robust validation of the model and new insights into the relationship between microcrack dynamics and observed acoustic signals.

The paper is organised as follows. First, the experimental setup used in our tests is briefly introduced in Section 2. Then, the DEM model and its calibration and validation procedure are described in Section 3. Section 4 compares the numerical results with the laboratory results. Finally, conclusions are drawn in Section 5.

2. Experimental investigations on bending beams

2.1. Materials and specimens

The materials used to produce the concrete in this study were Portland cement type CEM I 42.5R, sand (0/2 mm), fine aggregate (2/8 mm), coarse aggregate (8/16 mm), tap water and superplasticiser (0.7 % of the cement content). The proportions of the concrete mix are given in Table 1. Larger concrete prisms were first produced and then, after 28 days, the actual test specimens of 40 × 40 × 160 mm^3 were cut from them. A notch 4 mm wide and 7 mm deep was cut in the centre of each

Table 1
Mixture proportions of concrete.

Cement (kg/m^3)	Water (kg/m^3)	Sand 0/2 (kg/m^3)	Aggregate 2/8 (kg/m^3)	Aggregate 8/16 (kg/m^3)	Superplasticizer (kg/m^3)
330	165	710	664	500	2.31

specimen. Three specimens, hereafter referred to as beams #1, #2 and #3, were used for the experiments and simulations described in this paper.

2.2. Experimental setup and procedure

Three-point bending tests were performed to investigate the process of fracture behaviour of concrete beams. The experimental setup is given in Fig. 1a. The distance between supports was 120 mm (Fig. 1b). Bending was carried out using universal testing machine (Zwick Z10) with a displacement control with the rate of 0.05 mm/min. A preloading force was 20 N. The test lasted 360 s, up to displacement of 0.3 mm.

During the bending, the fracture evolution was characterized using the integrated acoustic emission (AE) and digital image correlation (DIC) methods. The front side of the beam was covered with a speckle pattern and the images were taken with a sampling frequency of 1 Hz using 3D DIC system equipped with two cameras with a resolution of 4096 × 3000 pixels. Crack mouth opening displacement (CMOD) was measured by virtual extensometer (see Fig. 1b), obtained from DIC measurements.

To register elastic waves caused by cracking, four multilayer piezoelectric sensors with dimensions 3x3x3 mm^3 were attached to the front side of the beam. This type of piezoelectric sensor is particularly suitable for the AE monitoring of small samples or samples with a limited amount of mounting space. According to the manufacturer's specification, the resonant frequency of the sensors used was greater than 500 kHz. Fig. 1b and Fig. 1c show the arrangement of the sensors (numbered S1 to S4). Acoustic emission signals were recorded using the AE system with a sampling rate of 10 MHz and a threshold of 30.1 dB.

3. Numerical modelling of plain concrete using DEM

3.1. Formulation of DEM for concrete

This study employed the discrete element method (DEM) using the open-source platform YADE [44,45]. DEM offers several advantages, including detailed descriptions of individual particles and a natural ability to account for damage and fracture between elements, making it particularly well suited to the study of concrete fracture. In DEM, particle motion (both translation and rotation) is governed by Newton's second law of motion using an explicit time-stepping scheme [46]. In this study, a simple linear contact law was used for normal compression, with brittle failure occurring when the normal tensile stress exceeded a critical value [47]. Tensile failure resulted in contact separation, while shear cohesion failure initiated contact slip and sliding according to the Coulomb friction law under normal compression. The mechanical responses of the DEM are presented in Fig. 2. The governing equations for particle motion and contact interactions are summarized below:

$$\boldsymbol{F}_n = K_n(U - U_o)\boldsymbol{N} \tag{1}$$

$$\boldsymbol{F}_s = \boldsymbol{F}_{s,prev} + K_s\Delta\boldsymbol{X}_s \tag{2}$$

$$K_n = E_{DEM}\frac{2R_AR_B}{R_A + R_B}, \quad \text{and} \quad K_s = \nu_{DEM}E_{DEM}\frac{2R_AR_B}{R_A + R_B} \tag{3}$$

$$\|\boldsymbol{F}_s\| - F_s^{\max} - \|\boldsymbol{F}_n\|\cdot\tan\mu \leqslant 0, \quad \text{(before contact breakage)} \tag{4}$$

$$\|\boldsymbol{F}_s\| - \|\boldsymbol{F}_n\|\cdot\tan\mu \leqslant 0, \quad \text{(after contact breakage)} \tag{5}$$

$$F_s^{\max} = CR^2, \quad \text{and} \quad F_n^{\min} = TR^2 \tag{6}$$

where $\boldsymbol{F}_n$ – the normal contact force, U – the overlap between discrete elements (U_o is an initial overlap that exists due to high compaction), $\boldsymbol{N}$ – the unit normal vector at the contact point, $\boldsymbol{F}_s$ – the tangential contact

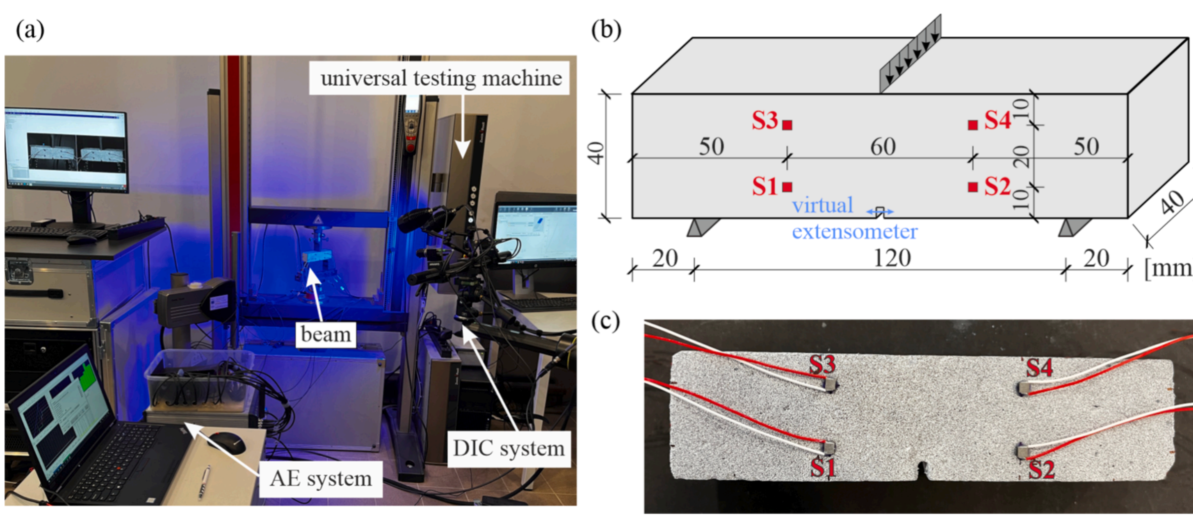

Fig. 1. (a) Experimental setup for integrated AE and DIC measurements; (b) the geometry of the beams and the location of PZT sensors; (c) the photograph of the front side of the beam before bending test.

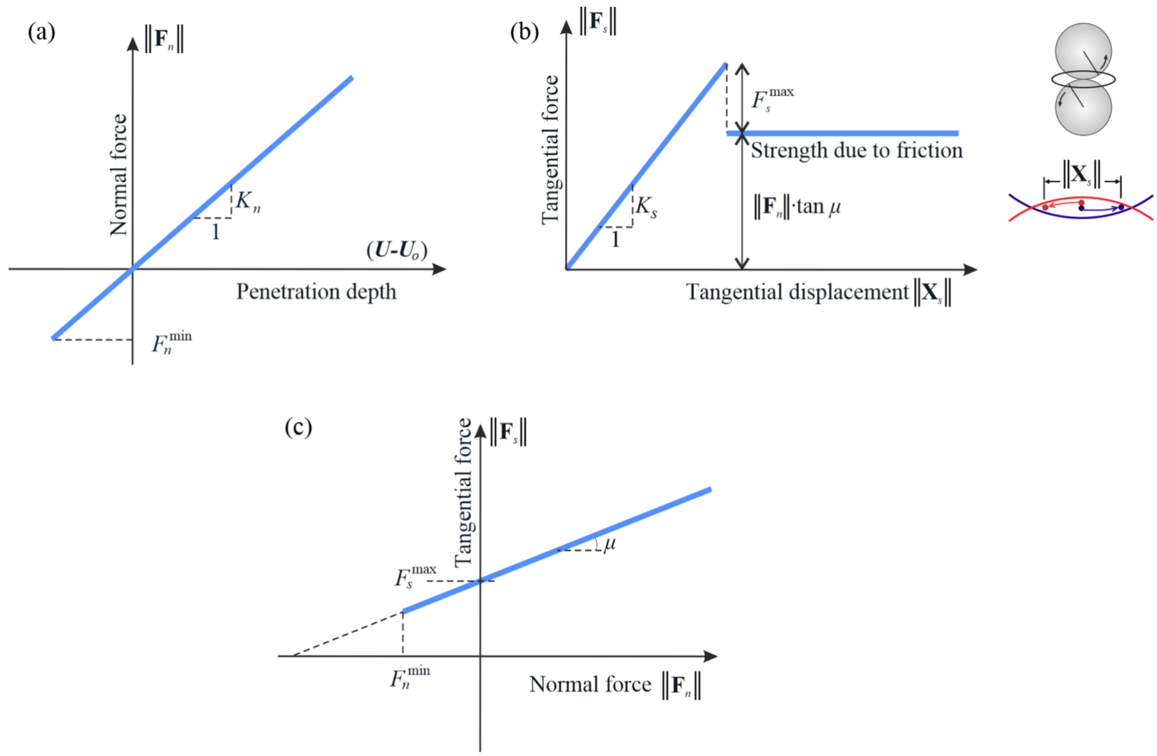

Fig. 2. Mechanical response of DEM: (a) normal contact model, (b) tangential contact model and (c) modified Mohr-Coulomb model [44,45].

force, $\boldsymbol{F}_{s,prev}$ – the tangential contact force in the previous iteration, $\Delta\boldsymbol{X}_s$ the relative tangential displacement increment, K_n – the normal contact stiffness, K_s – the tangential contact stiffness, E_{DEM} – the elastic modulus of the particle contact, υ_{DEM} – the stiffness ratio of particle contact ($\upsilon_{DEM} = K_s/K_n$), R – the smaller particle radius, R_A and R_B contacting particle radii, μ – the Coulomb inter-particle friction angle, $F_s^{\max}$ – the critical cohesive contact force, $F_n^{\min}$ – the minimum tensile force, C – the cohesive contact stress (maximum shear stress at a pressure equal to zero), and T – the tensile normal contact stress. If a cohesive joint (Eq. 6) between two elements vanished (whether in the normal or tangential direction) after crossing a critical threshold, damage was assumed. If any contacts between spheres were restored following failure, cohesion was considered absent (Eq. 6). The DEM model did not account for material softening.

The model presented here has been successfully used in previous static and dynamic [43] calculations. Experimental results have been effectively reproduced with satisfactory agreement in uniaxial compression [47,48], uniaxial tension [47], splitting [49,50], and bending tests [41,42,43]. In contrast to the previous acoustic emission study [39], this paper introduces a full 3D model. For studies involving acoustic emission, the adoption of a 3D model is preferable due to the need to measure acceleration signals in out-of-plane directions. In the 3D scenario, an increased occurrence of micro cracks is observed compared to 2D models, thus enhancing the investigation of damage mechanisms. Nonetheless, certain limitations were imposed in order to speed up the calculations. The concrete was modelled as a single-phase material, in contrast to other researchers, e.g. [51,52] or our previous study. Future work will employ a full 4-phase material model consisting of aggregate, interfacial transition zone, mortar, and air voids, thereby improving the representation of crack patterns [41,43,51,52]. Additionally, the interfacial transition zone can be modelled with a physical width, as in [53]. However, for the initial stages, the use of a single-phase material is deemed suitable for AE studies, as the focus lies primarily on the analysis of fracture initiation rather than exact crack morphology. The aim of the study was to introduce a model capable of reproducing the wave propagation phenomena that occur during fracture and the shape of the crack was not the primary focus of this study.

3.2. Numerical model of concrete beam

For numerical calculations, six main parameters must be selected: ρ, E_{DEM}, υ_{DEM}, μ, C and T. In this article, the numerical parameters were chosen to match those used in previous calculations [39], with only the mortar phase being utilized ($\rho = 2500$ kg/m^3, $E_{DEM} = 27.42$ GPa, $\upsilon_{DEM} = 0.17$, $\mu = 18^\circ$, $C = 48.46$ MPa and $T = 24.23$ MPa). The detailed calibration procedure was described in [54] and [39].

The size of the concrete specimen was the same as in the experiment ($40\times40\times160$ mm^3). It had a central notch with a dimension of 4×7 mm^2. Discrete spherical elements with diameters distributed linearly between 1 and 2 mm were employed, resulting in a total of 150,000 elements. These sphere dimensions were chosen to balance the need for accurate fracture reproduction while also optimizing computational efficiency. The YADE code does not yet support parallelization, so there are some limitations on the number of elements. The use of larger elements may slightly affect the global strength, but primarily affects only the final crack shape [47,48]. The initial porosity was set to 5%, consistent with the experimental conditions. Fig. 3 illustrates the initial geometry, highlighting the positions of PZT sensors (marked in yellow).

During the bending test in the DEM model, a constant vertical velocity of 0.5 mm/s was applied to the piston, while ensuring that the so-called inertia number remained below $I <$ 1e-4 to maintain quasi-static

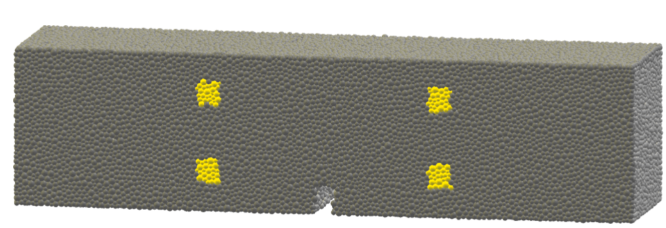

Fig. 3. Numerical 3D DEM model of concrete beam.

conditions [55]. The displacement of the piston and the crack mouth opening displacement (CMOD) were monitored throughout the test, along with tracking the number of broken contacts. Four distinct areas resembling multilayer piezoelectric transducers were modelled to replicate the experimental setup. The sensors in the numerical model were positioned identically to their locations in the laboratory tests, as illustrated in Figs. 1 and 3. In these designated regions, the average accelerations of the elements were calculated, considering them as the primary component of the elastic wave. The numerical DEM results were then compared with the experimental data in the following section to ensure a comprehensive analysis of the findings.

4. Results and discussion

Firstly, the macroscopic force-CMOD and force–displacement curves were compared in Fig. 4. The experimental load peaks had values of 1737.76 kN, 1865.3 kN and 1656.5 kN for beams #1, #2 and #3, respectively. The numerical results showed approximately a 33% higher strength (2327.72 N) compared to the mean laboratory value of 1753.19 N (with a standard deviation of 105.25 N and a coefficient of variation equal to 6%). The stiffness is also about 40% higher in the numerical analysis (with peaks at 0.158 mm and 0.23 mm for calculations and experiments, respectively). This discrepancy is due to the absence of aggregates and interfacial transitional zones (ITZs) in the model. Typically, the ITZ phase experiences a reduction of approximately 30% in stiffness and 35% in tensile and shear strength compared to cement-cement contacts. Consequently, the response without ITZs exhibits excessive strength and stiffness. However, this discrepancy does not significantly affect damage and energy release. However, the post-peak behaviour is similar and brittle. The force-CMOD curve also shows a significantly improved alignment (the numerical CMOD was calculated as the difference in notch width). The rapid drop visible in Fig. 4b was caused by using plain concrete specimens without any reinforcement and by piston-displacement control instead of CMOD control. In the numerical calculations, brittleness was also caused by the lack of microstructure, which resulted in more rapid final crack development.

The final crack shape observed in experiments appears much more curved due to the presence of aggregates (and ITZ) and air voids within the specimens (Fig. 5a-c). In contrast, the crack shape in the DEM calculations tends to be almost a straight line (Fig. 5d), because without taking into account the microstructure (such as aggregates and air voids, which act as attractors for the crack), the crack shape will solely conform to the stress criteria. Consequently, its shape will remain straight.

In Fig. 6, the evolution of the internal normal forces is depicted for

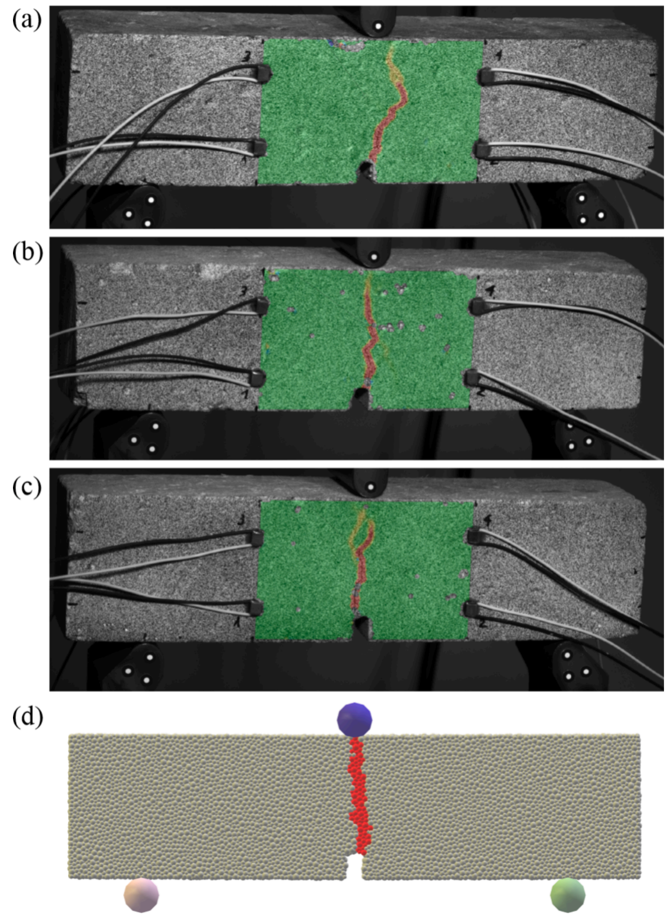

Fig. 5. Final cracking patterns in investigated specimens: (a) beam #1, (b) beam #2, (c) beam #3, (d) numerical 3D DEM beam model.

the middle cross-section only. The red and blue colours represent high compressive and tensile forces, respectively. Up to the peak, the forces exhibit typical behaviour for a bending beam, with strong compression below the piston and between the piston and supports, and strong tensile forces in the mid-bottom part of the beam (Fig. 6a). After the stress peak is reached, when a crack develops, the compressive forces remain close to the supports and piston, as well as inside the crack, where strong interlocking occurs (Fig. 6b).

Fig. 7 illustrates the evolution of the acceleration wave in the

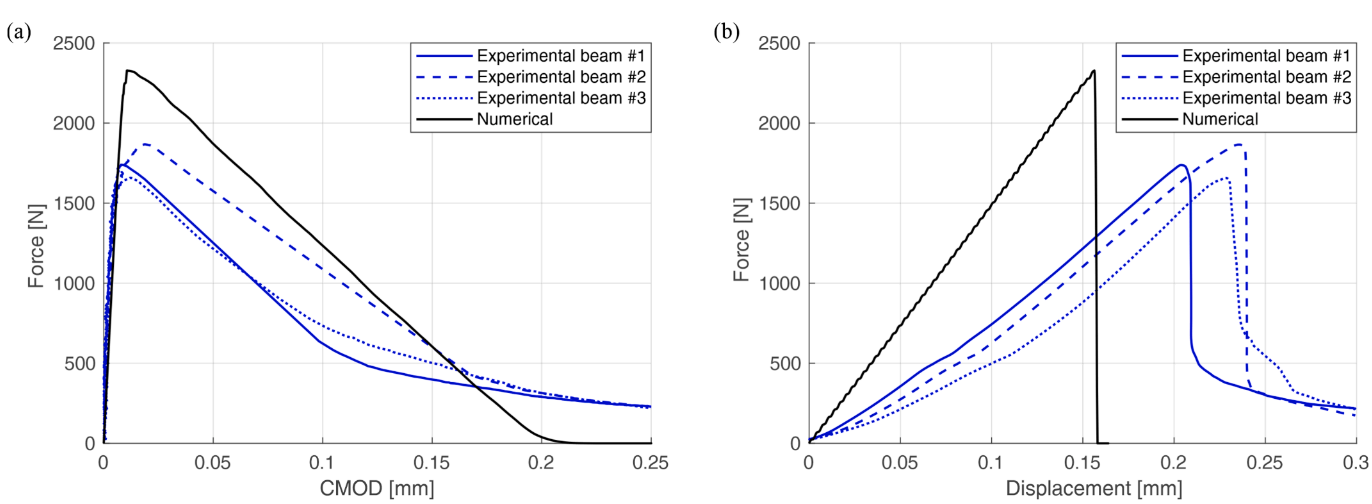

Fig. 4. Results from bending: (a) force-CMOD curves and (b) force–displacement curves for experimental beams #1–3 and numerical beam.

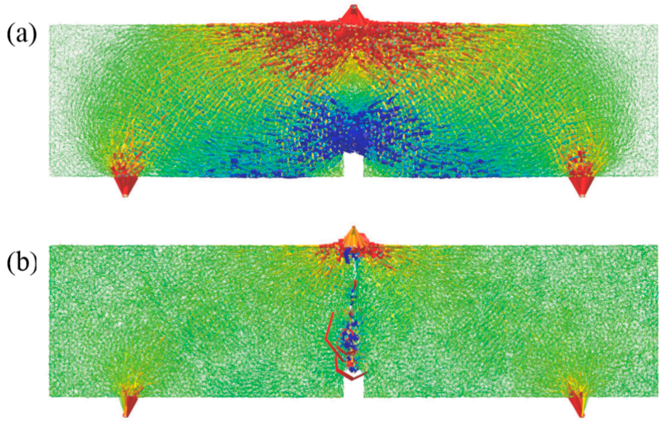

Fig. 6. Distribution of forces (red colour – compression, blue colour – tension) in 3D DEM model of concrete beam for different values of CMOD: (a) 0.008 mm, (b) 0.1 mm.

specimen. When contact is broken between two elements (forming a crack), the force at the contact is dismissed, and a new resultant force causes large accelerations of both elements. This acceleration propagates along neighbouring elements, creating an acceleration wave. This release of energy is similar to acoustic emission in reality. The white and black colours represent high (positive or negative) acceleration values equal to 1 mm/s^2, arbitrarily chosen for visibility. Only the mid cross-section of the specimen is shown. Initially, the acceleration field is homogeneous and small (Fig. 7a). When the contacts break, a visible wave propagates from the notch (Fig. 7b and c). Eventually, the wave

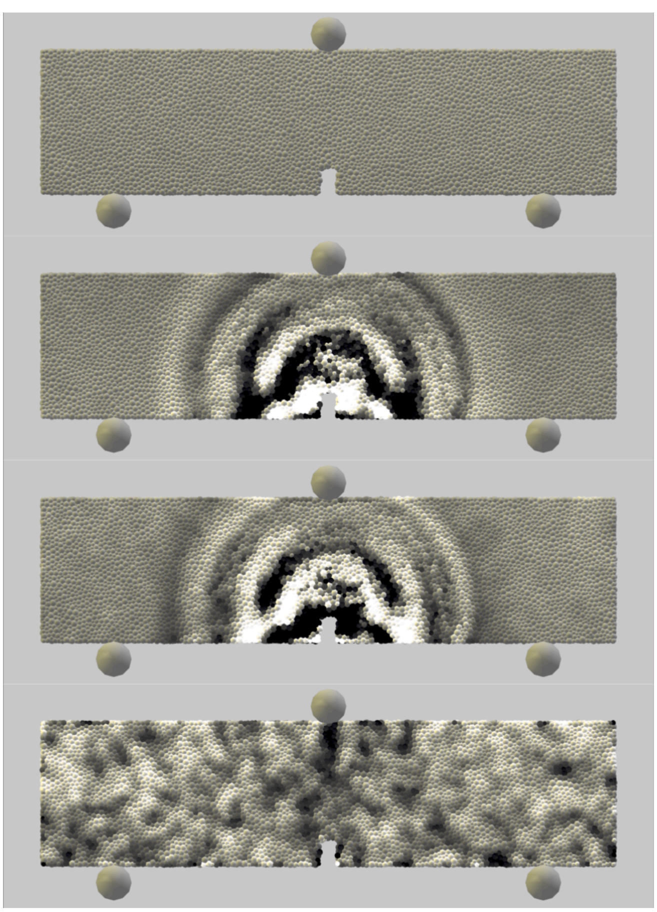

Fig. 7. Snapshots of acceleration field in the 3D DEM model.

propagates through the entire specimen and gradually decays (Fig. 7d).

In Fig. 8, acceleration signals (in the z direction, perpendicular to the beam surface) are presented. In the experiment, the signals were registered in a hit-based mode measurement. Then, all burst signals registered by sensors were assembled into one time vector containing all recorded transients. In the DEM simulation, the mean values of accelerations acting on the sensors are calculated and recorded every 0.0025 μm of CMOD opening. In both cases, small readings from sensors are visible before the stress peak is reached. The fluctuations in the signals correspond to micro-cracks and fracture developing inside the specimen. In the DEM calculations, due to the larger elements used in the model, the signals are more chaotic and persist almost throughout the entire duration. In contrast, in the experimental data, the signals are more concentrated in distinct periods. In the laboratory, micro-cracks appear more abruptly, whereas in the DEM they are more continuous. This difference is more apparent in the CMOD domain (Fig. 8, left column). In the displacement domain (Fig. 8, right column), it is evident that small micro-cracks occurred before the stress peak, while the main damage is measured around the peak values. Once again, in the DEM calculations, the damage becomes more evident after the stress peak, with the crack propagating more continuously. In the laboratory tests, however, the fluctuations appear as separate events.

An example of the energy distribution from sensor S1 is presented in Fig. 9, which shows the measured energy (green line), the cumulative energy (purple dashed line), together with the force curve (black line). In the experimental results, a significant energy jump occurs just after the main force peak (Fig. 9a,b), followed by only minor changes thereafter. The primary damage occurs at the stress peak. A different observation was made for the third beam (Fig. 9c), where the main crack occurred well after the peak (at a CMOD of 0.065 mm), but fracture continued to develop during the softening phase. Only some small values of elastic waves were observed before the stress peak. In the DEM calculations, the first energy jump was observed far before the stress peak, and the cumulative energy increased more steadily (Fig. 9d). It is evident that the main energy jumps also occurred just after the force peak, but its magnitude was more consistent with the subsequent ones, in contrast to the experimental results. A constant development of small cracks was observed until the final damage.

Similar observations were conducted for all the sensors (Fig. 10). For beams #1 and #2, a significant energy jump was observed just after the force peak. For beam #2, the differences between the sensors were extremely small (about 8%), whereas for beam #1, the difference was almost 40%. In beam #3, after a small jump following the stress peak, a substantial increase in energy occurred well after the force peak. Subsequently, the energy increased uniformly across all sensors. A similar result was observed in the DEM calculations where the initial energy jump coincided with the force peak. Thereafter, the energy increase was almost linear with minimal variation. In both experimental and numerical data, no significant differences were observed between the different sensors (although the values may differ, e.g., for beam #1, the trends of the curves remain similar). The DEM calculations revealed a more uniform behaviour due to the absence of large aggregates and macropores, with micro-cracks developing continuously. In the experiments (beams #1 and #2), the primary crack propagated rapidly at the stress peak, followed by sustained but minor damage.

The plot in Fig. 11 illustrates the relationship between the number of broken contacts in the CMOD domain for DEM calculations. Initially, a few contacts are broken far before the stress peak, which occurs at CMOD = 0.0054 mm (given that the peak is approximately 0.0105 mm). There is then a systematic increase in the number of broken contacts, following a non-linear shape, culminating in a final number of 4040 broken contacts, representing 0.45% of the initial total number of contacts.

In Fig. 12, both the broken contacts and the acceleration signals for sensor S1 are shown, including a zoomed-in section for a short period just before reaching the stress peak, corresponding to a piston

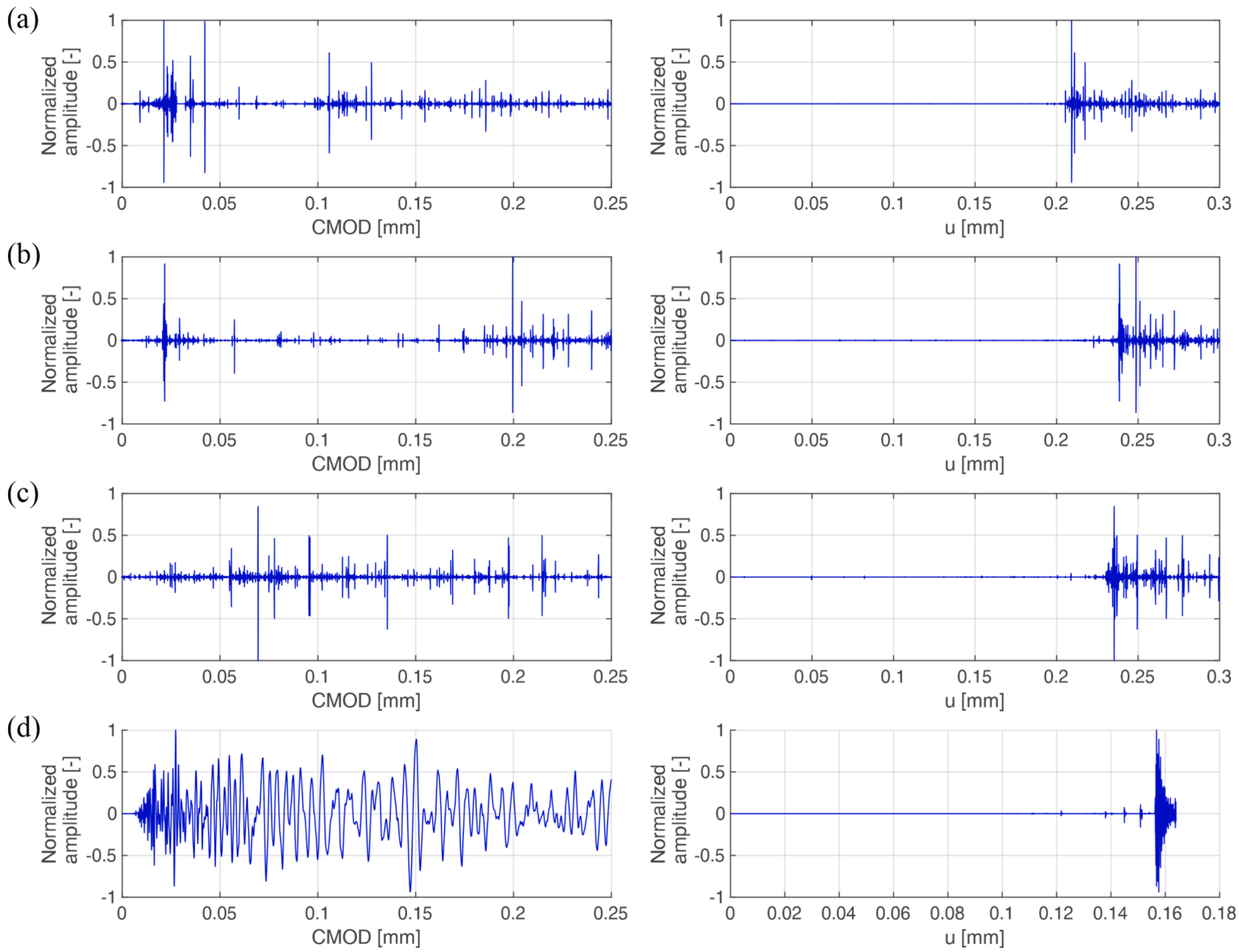

Fig. 8. Elastic wave signals acquired during experiments and in numerical simulations in the CMOD domain (first column) and in the displacement domain (second column): (a) beam #1, (b) beam #2, (c) beam #3, (d) numerical 3D DEM beam model.

displacement between 0.1 mm and 0.15 mm. For better visualization, the curve is presented on a piston displacement basis. It is noteworthy that after each fracture event (indicated by an increase in the number of broken contacts), the acceleration is recorded in all the sensors (Figs. 12 and 13). In Fig. 13, a very short piston displacement domain ($u = 0.001$ mm) is shown to better visualize the correlation between the data. There is a delay of several hundred iterations between the occurrence of the fracture and the measured jump in the sensors (Fig. 13), approximately 1.25e-5 s for bottom sensors (red and pink curves) and 1.45e-5 s for the upper ones (green and cyan curves), owing to their greater distance from the crack. Numerous acceleration jumps are clearly visible before the peak, coinciding with the development of micro-cracks within the specimen (Fig. 13). However, after the peak, the sensors exhibited chaotic and continuous outputs due to the brittle behaviour (rapid propagation of the crack) (Fig. 12a). Moreover, the energy released after the peak is notably higher.

The evolution of damage is depicted in Fig. 14. In the DEM calculations, the broken contacts (representing micro-cracks) are registered. In laboratory tests, digital image correlation (DIC) technique was used, which does not directly correspond to the contact breakages. The localisation began to appear before the stress peak for beams #2 and #3 (with no distinct localisation for beam #1). An important observation was made on beam #1 (Fig. 14a), where a significant energy jump was detected between CMOD = 0.015 mm and 0.019 mm, i.e., still in the nucleation phase of micro-cracks, indicating the very high sensitivity of the AE method for micro-damages. Subsequently, localization continued until the final shape, but no more such large energy jumps were observed. A less clear but similar observation was made in beam #2. In beam #3, both the released energy and the size of the localization increased simultaneously. The closest agreement in results was found between experimental beam #3 and numerical calculations. In both experiments and simulations, the observed jumps of elastic wave energy in the phase of micro-cracks (i.e., for the CMOD value smaller than 0.03 mm) indicating the moment of crack initiation. Since broken contacts are observed in the 3D DEM model of the beam, it can be concluded that the increase in AE energy is directly correlated to micro-cracks. It is evident that the appearance of microcracks and a rapid release of localized stress energy is connected with a loss of contact between particles.

In general, the AE appears to be a more accurate technique for tracking micro-cracks in larger elements, as demonstrated by DEM calculations, where each broken contact corresponds to an increase in energy (similar to beam #3). In small specimens, such as those used in this work, microstructure plays a significant role. For example, a large

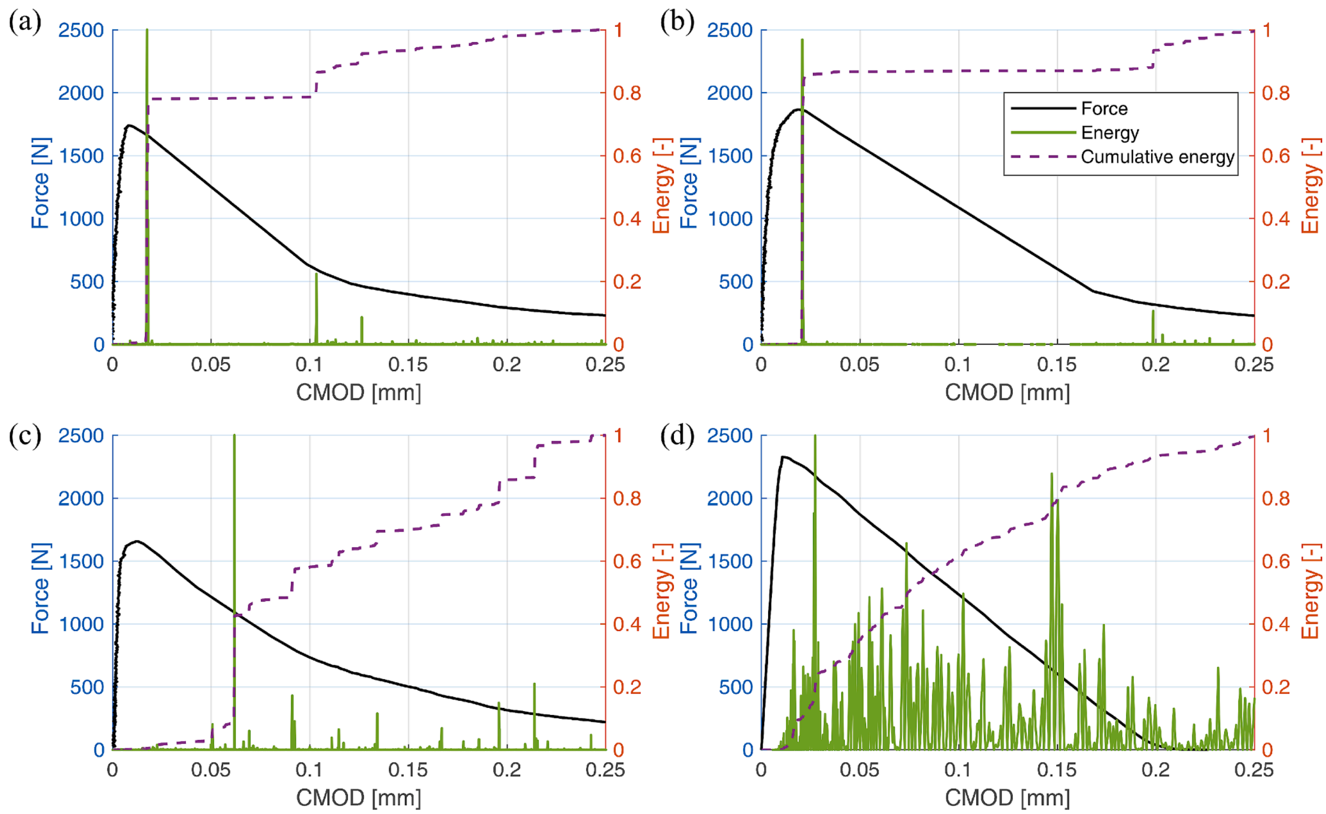

Fig. 9. Energy of signals registered by sensor S1 and the cumulative energy in the CMOD domain: (a) beam #1, (b) beam #2, (c) beam #3, (d) numerical 3D DEM beam model.

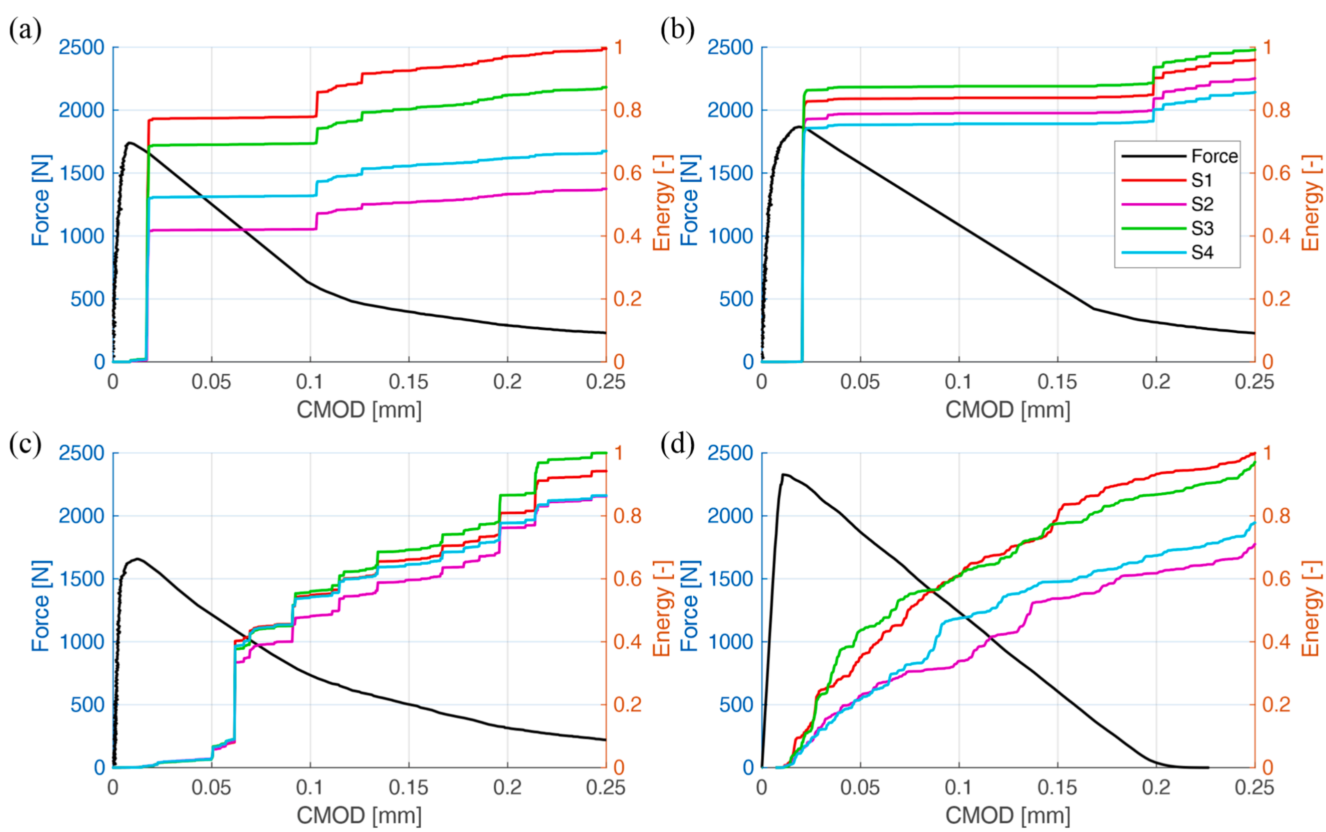

Fig. 10. Cumulative energy curves in the CMOD domain: (a) beam #1, (b) beam #2, (c) beam #3, (d) numerical 3D DEM beam model.

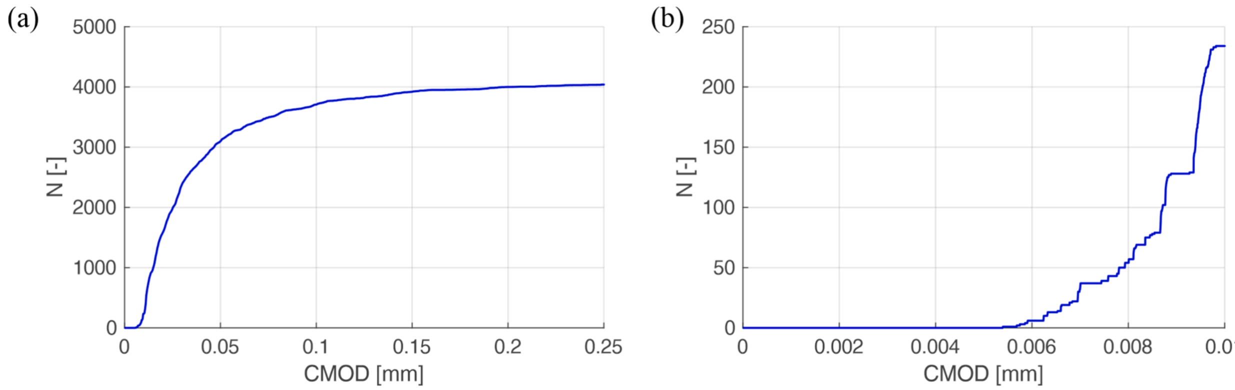

Fig. 11. The broken contacts in the specimen versus CMOD (a) whole test and (b) zoom in pre-peak part.

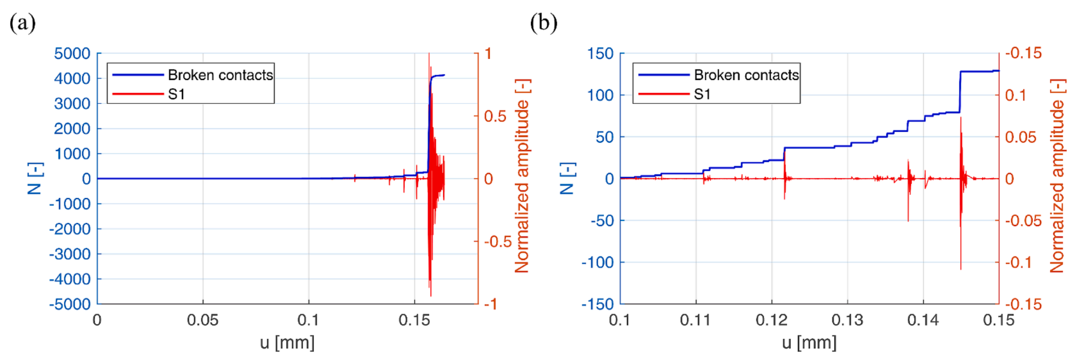

Fig. 12. The broken contacts in the specimen versus displacements, together with signal registered by sensor S1: (a) whole test and (b) zoom in pre-peak part.

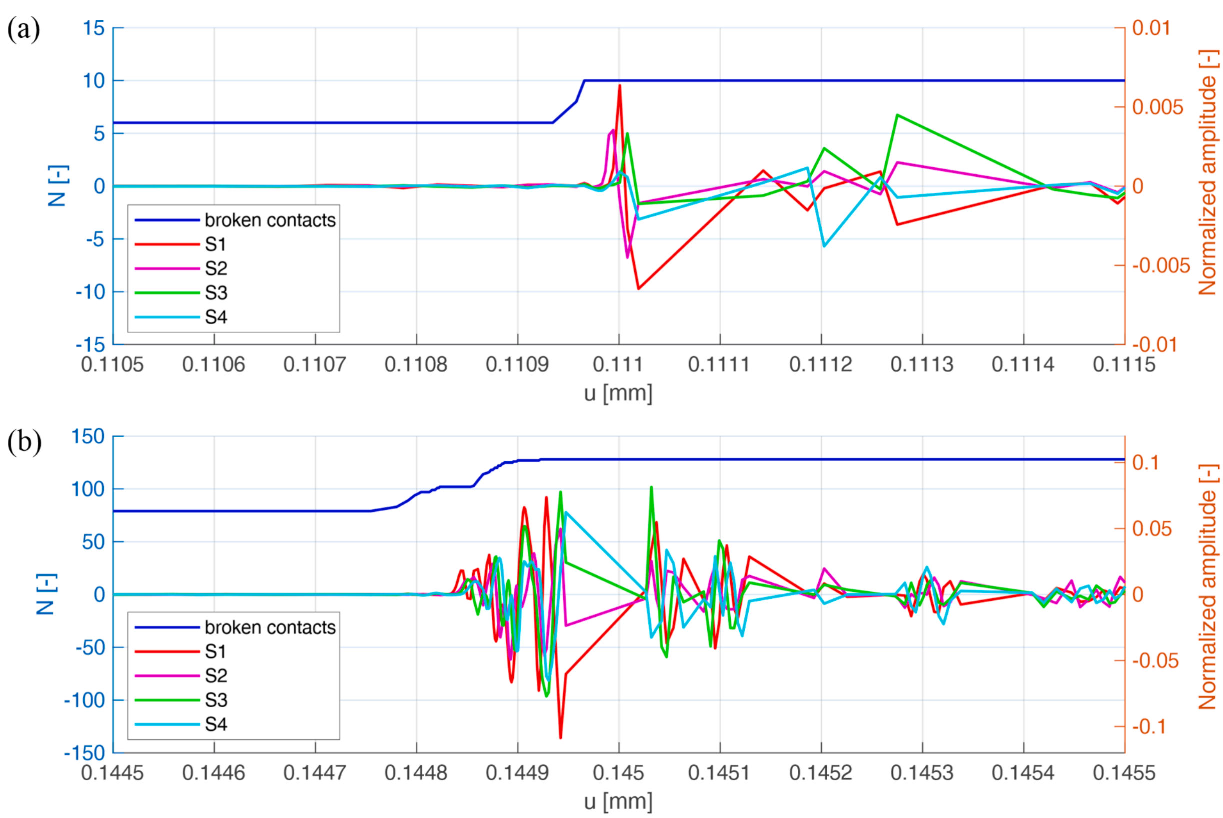

Fig. 13. The broken contacts in the specimen versus displacements, together with signal registered by all the sensors S1-S4 at selected displacements values: (a) 0.1105 mm to 0.1115 mm; (b) 0.1445 mm to 0.1455 mm.

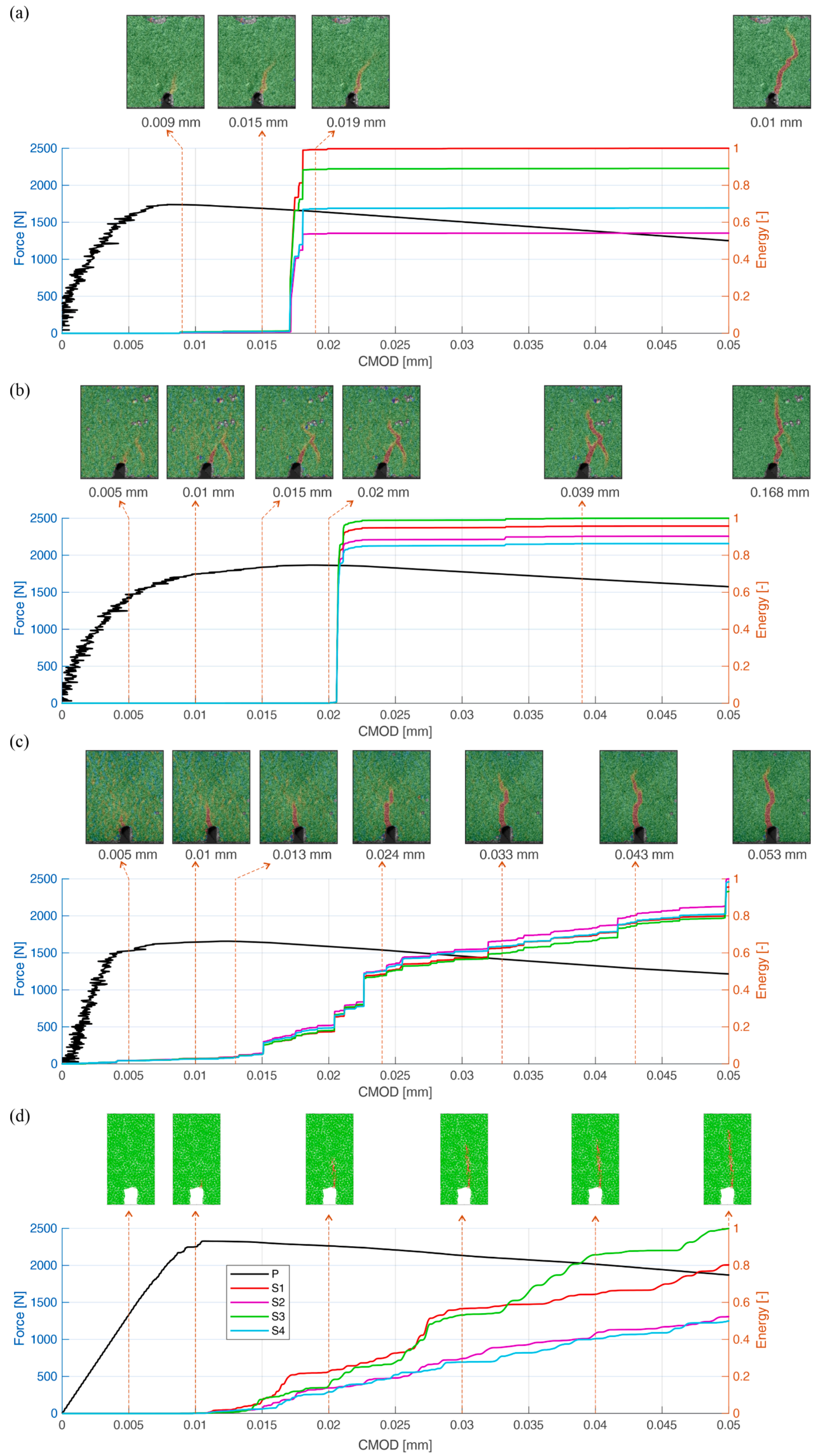

Fig. 14. Integrated results: force and cumulative energy–CMOD curves with images of cracking development: (a) beam #1, (b) beam #2, (c) beam #3, (d) numerical 3D DEM beam model.

aggregate positioned in the centre can result in a single large energy jump due to the sudden development of a large crack around the aggregate. In future studies, the microstructure will be accurately reproduced in the numerical model to ensure that these phenomena are captured.

5. Conclusions

This study focused on monitoring the fracture process of concrete beams under bending. Two non-destructive techniques, acoustic emission and digital image correlation, were used. DIC enabled observation of crack propagation on the specimen surface, while AE allowed for monitoring of the fracture process inside the specimen. The experiment was recreated using a three-dimensional discrete element method model to explore the feasibility of numerical modelling of the AE effects.

The 3D DEM simulations demonstrated reasonable agreement with the experimental results at both micro and macro levels. However, the global strength and stiffness of the specimens were higher than expected in the DEM due to the simplified representation lacking microstructural details such as aggregates, interfacial transition zones (ITZ), and air voids. Despite this limitation, the DEM model proved valuable for the calculation of concrete damage, fracture behaviour and the analysis of elastic waves generated by cracking.

Furthermore, numerical simulations allowed detailed analysis of the acoustic emission signals. The primary elastic wave signals obtained directly from the experiments were compared with DEM results, where accelerations were recorded using a full 3D model replicating the experimental conditions. Changes and jumps in the force curves due to micro-cracks corresponded to fluctuations in the AE event energy. Micro-crack initiation, considered as the loss of contact, resulted in detectable elastic waves in the sensors, consistent with experimental findings. It was proved that the appearance of microcracks and a rapid release of localized stress energy is associated with a loss of contact between particles of the concrete material.

Minor energy jumps were observed before reaching the stress peak, with significant values noted during the softening phase, notably in beam #3 where distinct steps were evident in the experimental data (while beams #1 and #2 showed limited increases in global energy). In the DEM calculations, a continuous increase was observed, indicating a smoother crack propagation attributed to the simplified representation without microstructural complexities.

This research represents a significant progress in understanding the mechanisms of elastic waves emitted during AE events and their interaction with micro- and macro-cracking in concrete under monotonic quasi-static loading, as elastic waves generated by fracture were analysed and compared. This understanding is crucial for early-stage crack detection in concrete structures. Future studies will focus on developing a precise 3D model that accurately captures elastic wave phenomena in heterogeneous materials and investigating the influence of aggregate shape and macro-pores in details.

CRediT authorship contribution statement

Michał Nitka: Writing – review & editing, Writing – original draft, Visualization, Methodology, Investigation, Formal analysis, Conceptualization. **Magdalena Rucka:** Writing – review & editing, Writing – original draft, Visualization, Project administration, Methodology, Investigation, Funding acquisition, Formal analysis, Conceptualization.

Declaration of competing interest

The authors declare that they have no known competing financial interests or personal relationships that could have appeared to influence the work reported in this paper.

Acknowledgements

The study was financed by the National Science Centre, Poland, under the project “Complex investigations of the development of micro- and macro-cracks in concrete members using elastic waves: experiments and discrete element method modelling” no 2019/35/B/ST8/01905.

Data availability

Data will be made available on request.

References

[1] Z.P. Bazant, J. Planas, Fracture and size effect in concrete and other quasibrittle materials, CRC Press, 1998.
[2] G. Lilliu, J.G.M. van Mier, 3D lattice type fracture model for concrete, Eng. Fract. Mech. 70 (2003) 927–941, https://doi.org/10.1111/j.1365-2966.2007.12569.x.
[3] I.M. Gitman, H. Askes, L.J. Sluys, Coupled-volume multi-scale modelling of quasi-brittle material, Eur. J. Mech. A/solids. 27 (2008) 302–327, https://doi.org/10.1016/j.euromechsol.2007.10.004.
[4] J. Tejchman, J. Bobiński, Continuous and discontinuous modelling of fracture in concrete using FEM, Springer, Berlin-Heidelberg, 2013.
[5] J. Helal, M. Sofi, P. Mendis, Non-destructive testing of concrete: A review of methods, Electron. J. Struct. Eng. 14 (2015) 97–105, https://doi.org/10.56748/ejse.141931.
[6] G. Lacidogna, G. Piana, F. Accornero, A. Carpinteri, Multi-technique damage monitoring of concrete beams: Acoustic emission, digital image correlation, dynamic identification, Constr. Build. Mater. 242 (2020) 118114, https://doi.org/10.1016/j.conbuildmat.2020.118114.
[7] J. Carette, S. Staquet, Monitoring and modelling the early age and hardening behaviour of eco-concrete through continuous non-destructive measurements: Part I. Hydration and apparent activation energy, Cem. Concr. Compos. 73 (2016) 10–18, https://doi.org/10.1016/j.cemconcomp.2016.07.002.
[8] A. Okeil, K. Matsumoto, K. Nagai, Investigation on local bond behavior in concrete and cement paste around a deformed bar by using DIC technique, Cem. Concr. Compos. 109 (2020) 103540, https://doi.org/10.1016/j.cemconcomp.2020.103540.
[9] O. Leibovich, A.N. Dancygier, D.Z. Yankelevsky, An innovative experimental procedure to study local rebar-concrete bond by direct observations and measurements, Exp. Mech. 56 (2016) 673–682, https://doi.org/10.1007/s11340-015-0116-z.
[10] T. Katsaga, E.G. Sherwood, M.P. Collins, R.P. Young, Acoustic emission imaging of shear failure in large reinforced concrete structures, Int. J. Fract. 148 (2007) 29–45, https://doi.org/10.1007/s10704-008-9174-x.
[11] D.G. Aggelis, D.V. Soulioti, N. Sapouridis, N.M. Barkoula, A.S. Paipetis, T. E. Matikas, Acoustic emission characterization of the fracture process in fibre reinforced concrete, Constr. Build. Mater. 25 (2011) 4126–4131, https://doi.org/10.1016/j.conbuildmat.2011.04.049.
[12] D.G. Aggelis, D.V. Soulioti, E.A. Gatselou, N.M. Barkoula, T.E. Matikas, Monitoring of the mechanical behavior of concrete with chemically treated steel fibers by acoustic emission, Constr. Build. Mater. 48 (2013) 1255–1260, https://doi.org/10.1016/j.conbuildmat.2012.06.066.
[13] R. Vidya Sagar, R.V. Prasad, B.K. Raghu Prasad, M.V.M.S. Rao, Microcracking and fracture process in cement mortar and concrete: A comparative study using acoustic emission technique, Exp. Mech. 53 (2013) 1161–1175, https://doi.org/10.1007/s11340-012-9708-z.
[14] S. Verbruggen, S. De Sutter, S. Iliopoulos, D.G. Aggelis, T. Tysmans, Experimental structural analysis of hybrid composite-concrete beams by digital image correlation (DIC) and acoustic emission (AE), J. Nondestruct. Eval. 35 (2016) 1–10, https://doi.org/10.1007/s10921-015-0321-9.
[15] G. Lacidogna, G. Piana, A. Carpinteri, Acoustic emission and modal frequency variation in concrete specimens under four-point bending, Appl. Sci. 7 (2017) 339, https://doi.org/10.3390/app7040339.
[16] P. Niewiadomski, J. Hoła, Failure process of compressed self-compacting concrete modified with nanoparticles assessed by acoustic emission method, Autom. Constr. 112 (2020), https://doi.org/10.1016/j.autcon.2020.103111.
[17] D. Logoń, K. Schabowicz, The recognition of the micro-events in cement composites and the identification of the destruction process using acoustic emission and sound spectrum, Materials (Basel). 13 (2020) 2988, https://doi.org/10.3390/ma13132988.
[18] J. Xu, S. Ashraf, S. Khan, X. Chen, A. Akbar, F. Farooq, Micro-cracking pattern recognition of hybrid CNTs/GNPs cement pastes under three-point bending loading using acoustic emission technique, J. Build. Eng. 42 (2021), https://doi.org/10.1016/j.jobe.2021.102816.
[19] S. Ashraf, S. Khan, V.K. Oad, Microcracking monitoring and damage detection of graphene nanoplatelets-cement composites based on acoustic emission technology, Case Stud. Constr. Mater. 18 (2023) e01844, https://doi.org/10.1016/j.cscm.2023.e01844.
[20] W. Suaris, J.G.M. Van Mier, Acoustic emission source characterization in concrete under biaxial loading, Mater. Struct. 28 (1995) 444–449, https://doi.org/10.1007/BF02473163.

[21] M. Ohtsu, T. Shiotani, M. Shigeishi, T. Kamada, S. Yuyama, T. Watanabe, T. Suzuki, J.G.M. van Mier, T. Vogel, C. Grosse, R. Helmerich, M.C. Forde, A. Moczko, D. Breysse, S.A. Ivanovich, A. Sajna, D. Aggelis, G. Lacidogna, Recommendation of RILEM TC 212-ACD: Acoustic emission and related NDE techniques for crack detection and damage evaluation in concrete: Measurement method for acoustic emission signals in concrete, Mater. Struct. Constr. 43 (2010) 1177–1181, https://doi.org/10.1617/s11527-010-9638-0.
[22] R. Vidya Sagar, B.K. Raghu Prasad, R.K. Singh, Laboratory investigations on concrete fracture using acoustic emission techniques, in: M. Ohtsu (Ed.), Acoust. Emiss. Relat. Non-Destructive Eval. Tech. Fract. Mech. Concr., Woodhead Publishing, Oxford, 2015: pp. 137–159. https://doi.org/10.1016/B978-1-78242-327-0.00007-6.
[23] X.Q. Zhou, H. Hao, Modelling of compressive behaviour of concrete-like materials at high strain rate, Int. J. Solids Struct. 45 (2008) 4648–4661, https://doi.org/10.1016/j.ijsolstr.2008.04.002.
[24] D.M. Cotsovos, M.N. Pavlović, Numerical investigation of concrete subjected to compressive impact loading. Part 1: A fundamental explanation for the apparent strength gain at high loading rates, Comput. Struct. 86 (2008) 145–163, https://doi.org/10.1016/j.compstruc.2007.05.014.
[25] Y. Lu, Z. Song, Z. Tu, Analysis of dynamic response of concrete using a mesoscale model incorporating 3D effects, Int. J. Prot. Struct. 1 (2010) 197–217, https://doi.org/10.1260/2041-4196.1.2.197.
[26] W.C. Zhu, X.D. Zhao, Y.M. Kang, C.H. Wei, J. Tian, Numerical simulation on the acoustic emission activities of concrete, Mater. Struct. 43 (2010) 633–650, https://doi.org/10.1617/s11527-009-9517-8.
[27] A. Lisjak, Q. Liu, Q. Zhao, O.K. Mahabadi, G. Grasselli, Numerical simulation of acoustic emission in brittle rocks by two-dimensional finite-discrete element analysis, Geophys. J. Int. 195 (2013) 423–443, https://doi.org/10.1093/gji/ggt221.
[28] X. Zhou, H. Zhao, Y. Xie, G. Long, X. Zeng, J. Li, S. Zhu, G. Ma, Mechanical behavior of bonded interface between steam-cured concrete and SCC under direct shear test: Experimental and numerical studies, J. Build. Eng. 63 (2023) 105517, https://doi.org/10.1016/j.jobe.2022.105517.
[29] X. Ren, C. Tang, Y. Xie, G. Long, G. Ma, H. Wang, Z. Tang, 3D mesoscale study on the effect of ITZ and aggregate properties on the fracture behaviors of concrete based on discrete element method, J. Build. Eng. 83 (2024) 108450, https://doi.org/10.1016/j.jobe.2024.108450.
[30] J. Rojek, N. Madan, S. Nosewicz, Micro–macro relationships in the simulation of wave propagation phenomenon using the discrete element method, Materials (Basel). 12 (2019) 4241, https://doi.org/10.3390/ma12244241.
[31] J. Hu, T. Ma, K. Ma, J. Xu, Three-dimensional discrete element simulation on degradation of air voids in double-layer porous asphalt pavement under traffic loading, Constr. Build. Mater. 313 (2021) 125570, https://doi.org/10.1016/j.conbuildmat.2021.125570.
[32] J. Hazzard, R. Young, Simulating acoustic emissions in bonded-particle models of rock, Int. J. Rock Mech. Min. Sci. 37 (2000) 867–872, https://doi.org/10.1016/S1365-1609(00)00017-4.
[33] S. Ji, S. Di, Discrete element modeling of acoustic emission in rock fracture, Theor. Appl. Mech. Lett. 3 (2013) 021009, https://doi.org/10.1063/2.1302109.
[34] Z. Chong, Q. Yao, X. Li, K. Shivakumar, Acoustic emission investigation on scale effect and anisotropy of jointed rock mass by the discrete element method, Arab. J. Geosci. 13 (2020), https://doi.org/10.1007/s12517-020-05303-z.
[35] L. Zhang, T. Ren, X. Li, L. Tan, Acoustic emission, damage and cracking evolution of intact coal under compressive loads: Experimental and discrete element modelling, Eng. Fract. Mech. 252 (2021) 107690, https://doi.org/10.1016/j.engfracmech.2021.107690.
[36] I. Iturrioz, G. Lacidogna, A. Carpinteri, Acoustic emission detection in concrete specimens: Experimental analysis and lattice model simulations, Int. J. Damage Mech. 23 (2014) 327–358, https://doi.org/10.1177/1056789513494232.
[37] A. Cheng, P. Shu, D. Deng, C. Zhou, S. Huang, Z. Ye, Microscopic acoustic emission simulation and fracture mechanism of cemented tailings backfill based on moment tensor theory, Constr. Build. Mater. 308 (2021) 125069, https://doi.org/10.1016/j.conbuildmat.2021.125069.
[38] R. Zhu, S.Y. Alam, A. Loukili, Relevance of displacement softening model in discrete element method to investigate structural and grain size scaling effect, Theor. Appl. Fract. Mech. 123 (2023) 103706, https://doi.org/10.1016/j.tafmec.2022.103706.
[39] M. Rucka, M. Knak, M. Nitka, A study on microcrack monitoring in concrete: discrete element method simulations of acoustic emission for non-destructive diagnostics, Eng. Fract. Mech. 293 (2023) 109718, https://doi.org/10.1016/j.engfracmech.2023.109718.
[40] C. Xie, L. Yuan, M. Zhao, Y. Jia, Study on failure mechanism of porous concrete based on acoustic emission and discrete element method, Constr. Build. Mater. 235 (2020) 117409, https://doi.org/10.1016/j.conbuildmat.2019.117409.
[41] M. Nitka, J. Tejchman, A three-dimensional meso-scale approach to concrete fracture based on combined DEM with X-ray μCT images, Cem. Concr. Res. 107 (2018) 11–29, https://doi.org/10.1016/j.cemconres.2018.02.006.
[42] M. Nitka, J. Tejchman, Comparative DEM calculations of fracture process in concrete considering real angular and artificial spherical aggregates, Eng. Fract. Mech. 239 (2020) 107309, https://doi.org/10.1016/j.engfracmech.2020.107309.
[43] M. Nitka, Static and dynamic concrete calculations: Breakable aggregates in DEM model, J. Build. Eng. 89 (2024), https://doi.org/10.1016/j.jobe.2024.109006.
[44] J. Kozicki, F.V. Donze, A new open-source software developer for numerical simulations using discrete modeling methods, Comput. Methods Appl. Mech. Eng. 197 (2008) 4429–4443.
[45] V. Šmilauer, B. Chareyre, Yade DEM Formulation, in: Yade Doc., The Yade Project, 1st ed., 2010. http://yade-dem.org/doc/formulation.html.
[46] P.A. Cundall, O.D.L. Strack, A discrete numerical model for granular assemblies, Geotechnique 29 (1979) 47–65.
[47] M. Nitka, J. Tejchman, Modelling of concrete behaviour in uniaxial compression and tension with DEM, Granul. Matter. 17 (2015) 145–164, https://doi.org/10.1007/s10035-015-0546-4.
[48] J. Suchorzewski, J. Tejchman, M. Nitka, Discrete element method simulations of fracture in concrete under uniaxial compression based on its real internal structure, Int. J. Damage Mech. 27 (2018) 578–607, https://doi.org/10.1177/1056789517690915.
[49] J. Suchorzewski, J. Tejchman, M. Nitka, Experimental and numerical investigations of concrete behaviour at meso-level during quasi-static splitting tension, Theor. Appl. Fract. Mech. 96 (2018) 720–739, https://doi.org/10.1016/j.tafmec.2017.10.011.
[50] J. Suchorzewski, M. Nitka, Size effect at aggregate level in microCT scans and DEM simulation – Splitting tensile test of concrete, Eng. Fract. Mech. 264 (2022) 108357, https://doi.org/10.1016/j.engfracmech.2022.108357.
[51] E.P. Prado, J.G.M. van Mier, Effect of particle structure on mode I fracture process in concrete, Eng. Fract. Mech. 70 (2003) 1793–1807, https://doi.org/10.1016/S0013-7944(03)00125-5.
[52] G. Lilliu, J.G.M. van Mier, On the relative use of micro-mechanical lattice analysis of 3-phase particle composites, Eng. Fract. Mech. 74 (2007) 1174–1189, https://doi.org/10.1016/j.engfracmech.2006.12.018.
[53] M. Nitka, J. Tejchman, Meso-mechanical modelling of damage in concrete using discrete element method with porous ITZs of defined width around aggregates, Eng. Fract. Mech. 231 (2020) 107029, https://doi.org/10.1016/j.engfracmech.2020.107029.
[54] M. Knak, M. Nitka, M. Rucka, Discrete element method modelling of elastic wave propagation in a meso-scale model of concrete, Ultrasonics 141 (2024) 107336, https://doi.org/10.1016/j.ultras.2024.107336.
[55] J.-N. Roux, F. Chevoir, Discrete numerical simulation and this mechanical behavior of granular materials, Bull. Des Lab. Des Ponts Chaussees. (2005) 109–138.